Enhanced Luminescence of Long-Wavelength Broadband Near-Infrared Germanate Phosphors

Shuya He, Yuanhong Liu,* Tongyu Gao, Ronghui Liu, Guantong Chen, Mobin Duan, and Min Cao

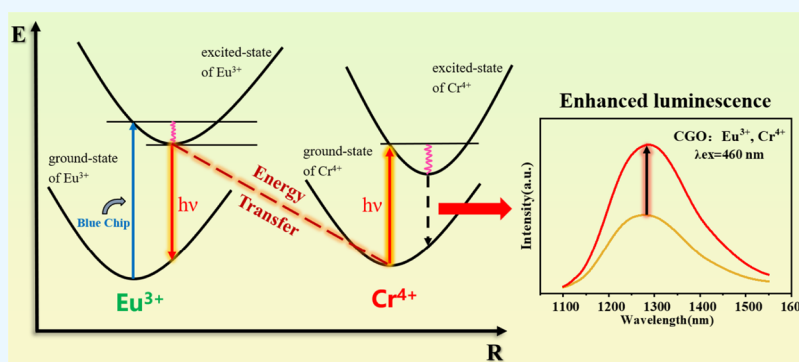Cite This: *ACS Omega* 2023, 8, 15698−15707

Read Online

ACCESS | Metrics & More | Article Recommendations | Supporting Information

ABSTRACT: Long-wavelength broadband near-infrared (NIR) phosphors have attracted considerable interest in the fields of medical cosmetology and organic detection because of their special emission band. Herein, Ca_2GeO_4(CGO): Cr^{4+} NIR phosphor, presenting a broadband emission with longer wavelength ranging from 1100 to 1600 nm, has been synthesized. Further, the luminescence intensity and quantum efficiency of Cr^{4+} could be obviously improved via the energy transfer from Eu^{3+} to Cr^{4+}. The energy transfer is dominated by the dipole−dipole mechanism, which can be inferred from the spectra and the decay curves. Furthermore, in order to evaluate the potential application, an NIR phosphor-converted light-emitting diode (pc-LED) based on blue chip has been prepared. Consequently, CGO: Eu^{3+}, Cr^{4+} exhibits proper output power and wider half-width than the NIR LED chip, indicating its great prospect for long-wavelength NIR pc-LED applications.

1. INTRODUCTION

Long-wavelength near-infrared (NIR), especially over 1100 nm, has promising applications in medical cosmetology, organic detection, fluorescence imaging, and other fields.[1−3] Long-wavelength NIR light has a unique ability to securely and nondestructively penetrate biological tissues, which have weaker absorption, scattering, and autofluorescence to long-wavelength NIR light and are highly competitive in the field of fluorescence imaging.[4] Moreover, long-wavelength NIR light has characteristic performance on organic groups, where it can detect and analyze water, fats, proteins, and other compositions based on the characteristic absorption and reflection spectra of elemental bonds. For example, NIR spectroscopy makes use of the NIR light as a nondestructive and real-time monitoring analytical tool in testing technology in order to detect and analyze the compositions. More information can be obtained by using a wider band.[5] Therefore, an NIR light source, as broad as possible, is critically needed for effective performance. The NIR luminescence is mainly realized with semiconductor chips in common NIR light-emitting diodes (NIR-LEDs). However, in contrast to long-wavelength NIR chips, which have a narrow spectrum and are of high cost and difficult to fabricate, the phosphor-converted LEDs (pc-LEDs) proposed

in late 2016 achieve NIR emission by combining blue chips with broadband NIR phosphors.[6] Due to their low cost, long lifetime, quick response speed, and extensive applicability, pc-LEDs have attracted great attention. Obviously, NIR phosphors play a crucial role in NIR pc-LEDs, and the development of high-performance long-wavelength broadband NIR phosphor is urgently needed.

Cr^{3+}-doped broadband NIR phosphors can properly match blue LED chips and have wavelength tunable performance. Cr^{3+} can achieve deep red and NIR broadband luminescence between 700 and 1000 nm but cannot reach the long wavelength NIR band around 1300 nm due to the limitation of crystal field conditions.[7−9] The Cr^{4+}-doped long-wavelength NIR phosphors have an excitation in each of the blue and red bands. There is no major change in the shape of the emission

spectrum under both excitation wavelengths, exhibiting broadband emission near 1300 nm. Hence, it has the potential to package NIR pc-LEDs with blue chips. The luminescence type of Cr^{4+} mainly depends on the crystal field strength of the host lattice: in the strong field site, a narrow band of $^1E \rightarrow {}^3A_2$ spin-forbidden luminescence is generated, and in the weak field, a wide band of $^3T_2 \rightarrow {}^3A_2$ spin-permitted luminescence (1000−1600 nm) is generated.[10−12]

The olivine matrix has tetrahedral sites for Cr^{4+} substitution.[13] Mg_2SiO_4: Cr^{4+} is the first NIR tunable solid-state laser material based on Cr^{4+} research. Subsequently, on the basis of Mg_2SiO_4 structure, a new Cr^{4+}-doped laser crystal Ca_2GeO_4(CGO): Cr^{4+} was prepared by replacing Mg^{2+} with Ca^{2+} and Si^{4+} with Ge^{4+}, whose tunable emission is in the range of 1200−1700 nm in the NIR spectrum.[14−17] Bykov et al.[15] obtained single crystals of CGO: Cr^{4+} using the flux growth technique and pulling method. CGO: Cr^{4+} exhibited broadband NIR emission in the 1000−1600 nm range with a peak position of 1290 nm at 670 nm excitation. Li C's[18] group grew CGO: Cr^{4+} crystals by the flux method. The emission spectrum obtained by 824 nm excitation was between 1000 and 1600 nm, with the maximum emission peak of 1317 nm and the full-width at half maximum (FWHM) of 201 nm. In addition to crystalline materials, phosphors with Cr^{4+} as the luminous center began to come into public view, such as $Ca_2Al_2SiO_7$: Cr^{4+} (1100−1500 nm),[19] $Mg_{14}Ge_5O_{24}$: Cr^{3+}, Cr^{4+} (1000−1400 nm),[20] Li_2ZnGeO_4: Cr^{4+} (1000−1500 nm),[21] and so forth. Recently, Ye[22] synthesized CGO: Cr^{4+} phosphors with 1000−1700 nm emission and a peak position of 1270 nm for ethanol detection.

So far, many researchers focused on crystalline materials for tunable lasers with Cr^{4+} as the luminous center. The study of Cr^{4+}-doped NIR phosphors is particularly imperfect and suffers from low luminosity efficiency, which cannot meet the application requirements. As one of the most special sensitizers, the luminescence of Eu^{3+} originates from the f−f forbidden transition and is less sensitive to the surrounding environment. It offers strong red emission under efficient blue excitation, which has great potential in optimizing the luminescence performance of activated Cr^{4+} ions.[23−25] In this paper, we study the olivine structure, photoluminescence characteristics, and energy-transfer mechanism of CGO: xEu^{3+}, yCr^{4+} phosphors. The luminescence intensity of Cr^{4+} is enhanced by energy transfer from Eu^{3+} to Cr^{4+}, and the mechanism is elucidated based on photoluminescence excitation spectra (PLE), photoluminescence spectra (PL), and decay lifetime curves. Finally, the temperature-dependent luminescence properties and the potential practical applications of NIR pc-LEDs are also discussed to evaluate the optical performance comprehensively.

2. EXPERIMENT

2.1. Materials and Synthesis.
Stoichiometric amounts of $CaCO_3$, GeO_2, Cr_2O_3, and Eu_2O_3 were used as raw materials, weighed according to the stoichiometric ratio, and well ground in an agate mortar until evenly mixed. The mixed powder was transferred to alumina crucibles and sintered at 1300 °C for 3 h through high-temperature solid-state reaction in an air atmosphere. After cooling to room temperature, all samples were reground in an agate mortar to obtain a series of Ca_2GeO_4(CGO): xEu^{3+}, yCr^{4+} ($0 \leq x \leq 0.013$, $0 \leq y \leq 0.013$) phosphors.

2.2. Characterization.
Phase purity was analyzed by X-ray diffraction (XRD, Japan) over the 2θ range from 15 to 70° with Co Kα radiation ($\lambda = 0.178892$ nm), and the operating voltage and current were 40 kV and 120 mA, respectively. Rietveld structure fineness of samples was measured in the angle range of $10° < 2\theta < 110°$. The crystal structure schematic of the CGO host was drawn in VESTA (visualization for electronic and structural analysis) and performed by the Rietveld method using the GSAS (general structure analysis system) program.[26] Excitation spectra and emission spectra were recorded using a FluoroMax4NIR spectrometer (HORIBA Scientific, Japan) equipped with a 200 W Xe lamp. The luminescence intensity of the samples was measured using a HAAS-2000 high precision fast spectral radiometer (EVERFINE, Hangzhou) at room temperature (25 °C). Laser radiation was used as the excitation source to measure fluorescence decay curves and temperature-dependent emission spectra by a FLS980 lifetime and steady-state spectrometer (Edinburgh Instruments Ltd., UK). NIR internal quantum yield (QY) was measured by a FLS980 lifetime and steady-state spectrometer (Edinburgh Instruments Ltd., UK) using a 450 W xenon lamp.

3. RESULTS AND DISCUSSION

3.1. Structural Characterization.
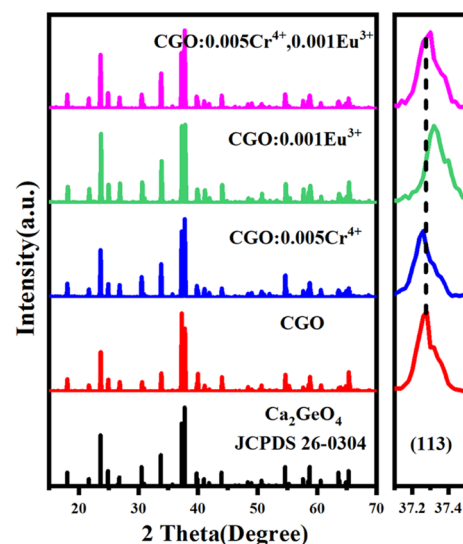The XRD patterns of CGO: xEu^{3+}, yCr^{4+} phosphors are shown in Figure 1. All X-ray

Figure 1. XRD patterns of CGO: xEu^{3+}, yCr^{4+}.

powder diffraction patterns are consistent with the corresponding standard data of the Ca_2GeO_4 crystal phase (JCPDS card No. 26-0304). The $2\theta = 37.1-37.5°$ diffraction peak of CGO: xEu^{3+}, yCr^{4+} belonging to the (113) crystal plane is amplified and compared. It is found that the diffraction peak shifts toward lower angles with the doping of Cr^{4+} and shifts toward higher angles with the doping of Eu^{3+} since the Ge^{4+} (0.39 A, CN = 4) ions are substituted by larger radii ions Cr^{4+} (0.41 A, CN = 4), while the Ca^{2+} (0.99 A, CN = 6) ions are smaller than Eu^{3+} (0.947 A, CN = 6).[27] This finding reveals that Cr^{4+} and Eu^{3+} successfully enter the cell.

Olivine structure CGO crystal belongs to the orthorhombic system with the space group *Pnma* (62).[28] In this configuration, there are two nonequivalent Ca atomic sites and one Ge atomic site, where Ca1 is located at the inversion
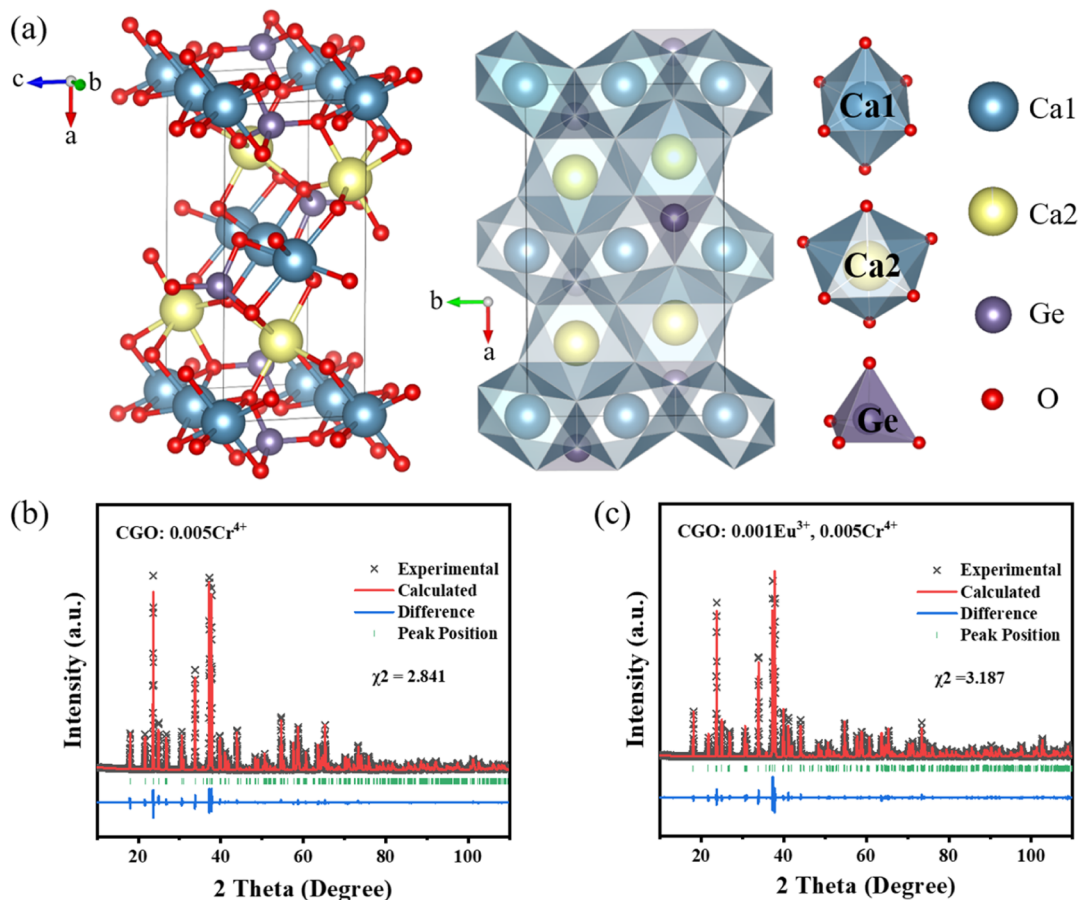
Figure 2. (a) Crystal structure schematic illustration and cation coordination diagram of CGO. (b) Rietveld refinement of CGO: $0.005Cr^{4+}$. (c) Rietveld refinement of CGO: $0.001Eu^{3+}$, $0.005Cr^{4+}$.

Table 1. Structural Refinement Parameters with Eu Occupying Ca1, Ca2, and Ca1−Ca2 Sites

	Ca1	Ca2	Ca1−Ca2
polyhedron type	octahedron	octahedron	octahedron
R_{wp} (%)	11.92	12.12	11.80
R_p (%)	8.28	8.32	8.03
χ^2	3.093	3.104	3.019

center and Ca2 and Ge are located in the mirror plane. Each Ca is coordinated with six oxygens in its surroundings to form an octahedron, while each Ge is coordinated with four oxygens to form a tetrahedron (Figure 2a). Considering the valence

equilibrium and ionic radius, Cr preferentially tends to replace Ge (Cr^{4+} = 0.41 Å, Ge^{4+} = 0.39 Å), while Eu^{3+} is more likely to replace Ca^{2+} randomly (Eu^{3+} = 0.947 Å, Ca^{2+} = 0.99 Å). To evaluate the phase structure of the prepared phosphors, three models with Ca1, Ca2, and Ca1−Ca2 sites occupied by Eu were constructed, and the structure refinement was performed. The results are shown in Table 1. Compared with the R_{wp} and χ^2 of three models, they are all very similar, so that it is considered that the two Ca sites have a similar influence on Eu. Moreover, Rietveld refinement of CGO: Cr^{4+} and CGO: Eu^{3+}, Cr^{4+} have been implemented by GSAS program with Cr occupying Ge and Eu occupying Ca. As shown in Figure 2b,c,
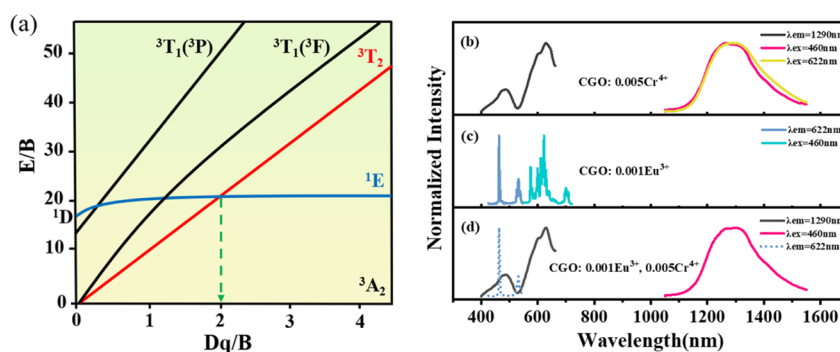

Figure 3. (a) Tanabe−Sugano diagram of Cr^{4+} in the tetrahedron. PLE and PL spectra of (b) CGO: Cr^{4+}, (c) CGO: Eu^{3+}, and (d) CGO: Eu^{3+}, Cr^{4+}.
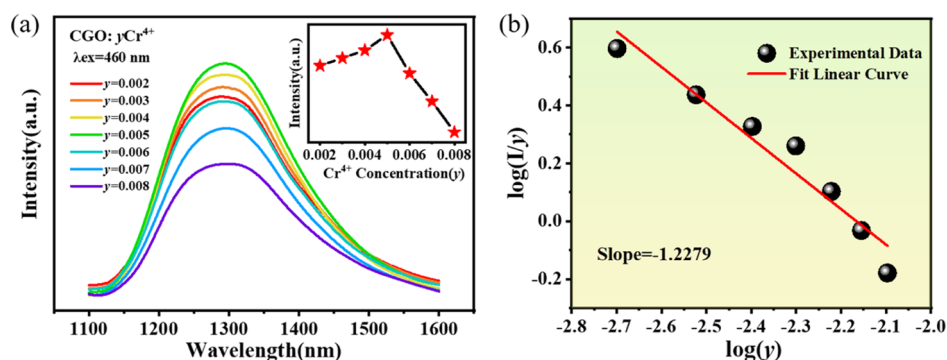
Figure 4. (a) PL spectra of CGO: yCr^{4+} ($0 \le y \le 0.008$), and concentration dependence of peak intensity at 1290 nm is inserted. (b) Linear fitting relationship of log(I/y) and log(y).

Table 2. Luminescence Properties of Several Cr⁴⁺-Doped NIR Phosphors

| Phosphor	EX (nm)	EM (nm)	FWHM (nm)	Application
Mg$_2$SiO$_4$: Cr^{3+}-Cr^{4+}	450	1120		absorption spectrometry of agricultural products[5]
Ca$_2$Al$_2$SiO$_7$: Cr^{4+}	730	1230		NIR nano-thermometers[19]
Mg$_{14}$Ge$_5$O$_{24}$: Cr^{3+}-Cr^{4+}	670	1240	256	biological detection[20]
Mg$_2$GeO$_4$: Cr^{3+}-Cr^{4+}	578	1190		food detection[38]
Ca$_2$GeO$_4$: Cr^{4+}	489	1270	215	ethanol detection[22]
Li$_2$ZnGeO$_4$: Cr^{4+}	646	1218	220	non-destructive examination and bioimaging[21]
Ca$_2$GeO$_4$: Eu^{3+}, Cr^{4+}	460	1290	200	organic detection and fluorescence imaging
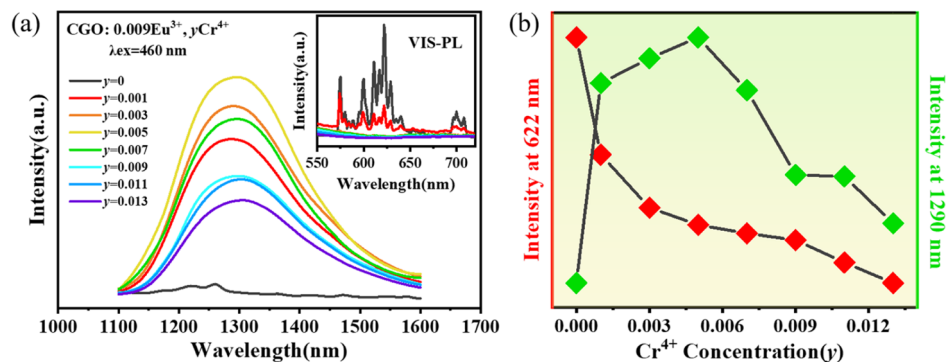
Figure 5. (a) PL spectra of CGO: 0.009Eu^{3+}, yCr^{4+} ($0 \le y \le 0.013$). The inset shows the enlarged view of visible emission spectra in the range of 550−720 nm. (b) Luminescence intensity of Eu^{3+} (622 nm) and Cr^{4+} (1290 nm) in CGO: 0.009Eu^{3+}, yCr^{4+} ($0 \le y \le 0.013$) varies with an increase of Cr^{4+} concentration.

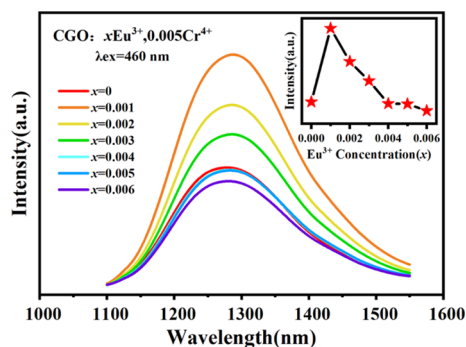**Figure 6.** PL spectra of CGO: xEu^{3+}, 0.005Cr^{4+} ($0 \le x \le 0.006$). The inset shows the luminescence intensity as a function of Eu^{3+} doping concentration.

the refinement converged to R_{wp} = 11.45%, χ^2 = 2.841(CGO: 0.005Cr^{4+}) and R_{wp} = 12.54%, χ^2 = 3.187 (CGO: 0.001Eu^{3+}, 0.005Cr^{4+}). The final results show that the synthesized phosphors are pure phase, and the refinement results are reliable.

3.2. Luminescence Properties of Cr⁴⁺-Doped and Eu³⁺-Doped CGO. The Tanabe−Sugano diagram of Cr^{4+} in the tetrahedron is shown in Figure 3a. It can be seen that the energy level position of ^{3}T$_2$ increases with the increase of the crystal field strength (Dq/B), while the position of the ^{1}E energy level has no obvious changes. The value of Dq/B at the intersection position of ^{3}T$_2$ and ^{1}E energy levels is about 2.[10−12] When Dq/B < 2, the crystal field is a weak field, and the ^{3}T$_2$ energy level is below the ^{1}E energy level. The spin-allowed transition of ^{3}T$_2$ → ^{3}A$_2$ occurs, accompanied by a wide emission band around 1300 nm, which is quite different from Cr^{3+}. What is more, the luminescence of Cr^{4+} in phosphors is rarely reported, and the olivine matrix may be an important host for Cr^{4+} emission because it has suitable ionic radii for Cr^{4+} and no suitable lattice sites for Cr^{3+} substitution.[20]

Upon 460 or 622 nm radiation excitation, CGO: 0.005Cr^{4+} shows a broad NIR emission peak at 1290 nm that superimposes on the emission ranging from 1000 to 1600
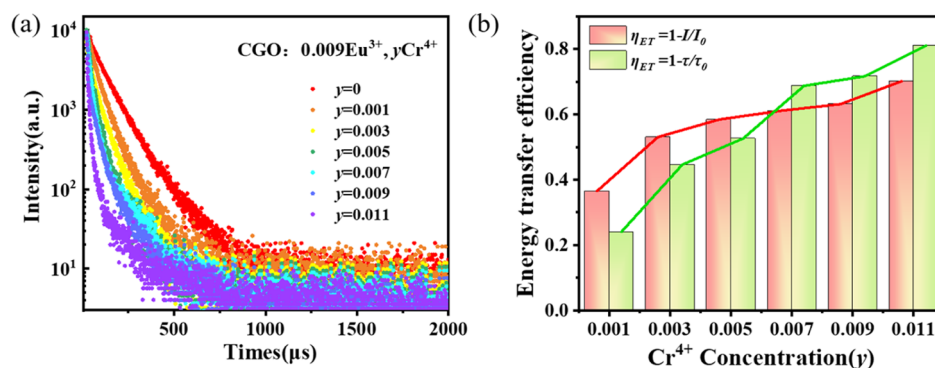
Figure 7. (a) Decay curves of CGO: $0.009Eu^{3+}$, yCr^{4+} ($0 \leq y \leq 0.011$) monitored at 622 nm under 460 nm excitation. (b) Energy-transfer efficiency calculated by formulas 3 and (4).
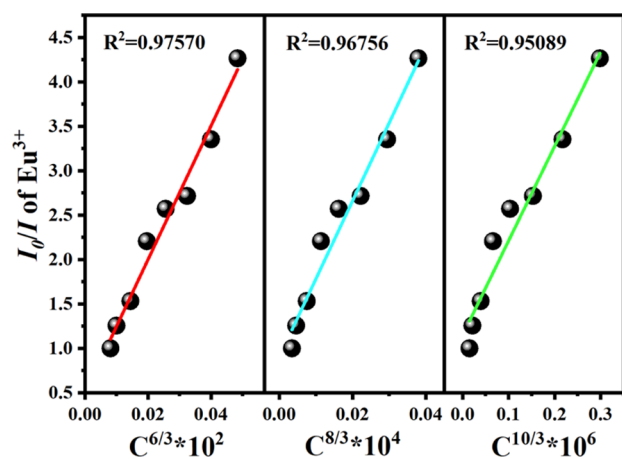

Figure 8. Linear fitting relationship between I_0/I and $C^{n/3}$ ($n = 6,8,10$).

nm (Figure 3b). Both excitation wavelengths have extremely high emission intensities, and there is no major change in the shape of the emission spectrum, which indicates that these NIR emissions should originate from the relaxations of the

same excited states.[29] The associated PLE spectrum consists of two distinct bands from 400 to 530 nm and 530 to 680 nm, originating from the $^3A_2 \rightarrow {}^3T_1(^3P)$ and $^3A_2 \rightarrow {}^3T_1(^3F)$ transitions, respectively. Importantly, the excitation bands can well match the commercial blue chips, demonstrating the potential for applications in blue-pumped LEDs.

A series of CGO: yCr^{4+} ($0 \leq y \leq 0.008$) phosphors have been prepared to obtain the best composition. As shown in Figure 4a, the intensity peak is at $y = 0.005$. Further increasing the concentration of Cr^{4+} results in a decrease of the intensity, which can be ascribed to the concentration quenching caused by nonradiative energy transfer. Depending on the critical concentration, the critical distance R_c between Cr^{4+} ions can be calculated as follows[30,31]

$$R_c = 2\left(\frac{3V}{4\pi x_c N}\right)^{1/3}$$

$$(1)$$

Here, V corresponds to the cell volume, x_c is the critical concentration of doped ions, and N refers to the number of Cr^{4+} in one unit cell. For the CGO matrix, the critical distance $R_c = 33.815$ Å was calculated from $V = 404.908$ Å^3, $x_c = 0.005$, $N = 4$, which is much larger than 5 Å, indicating that the

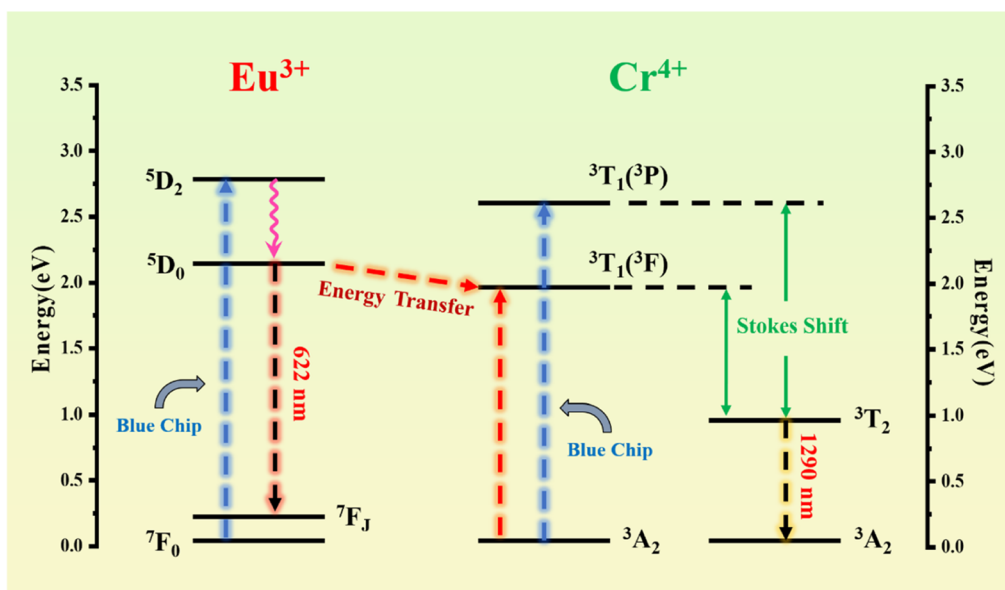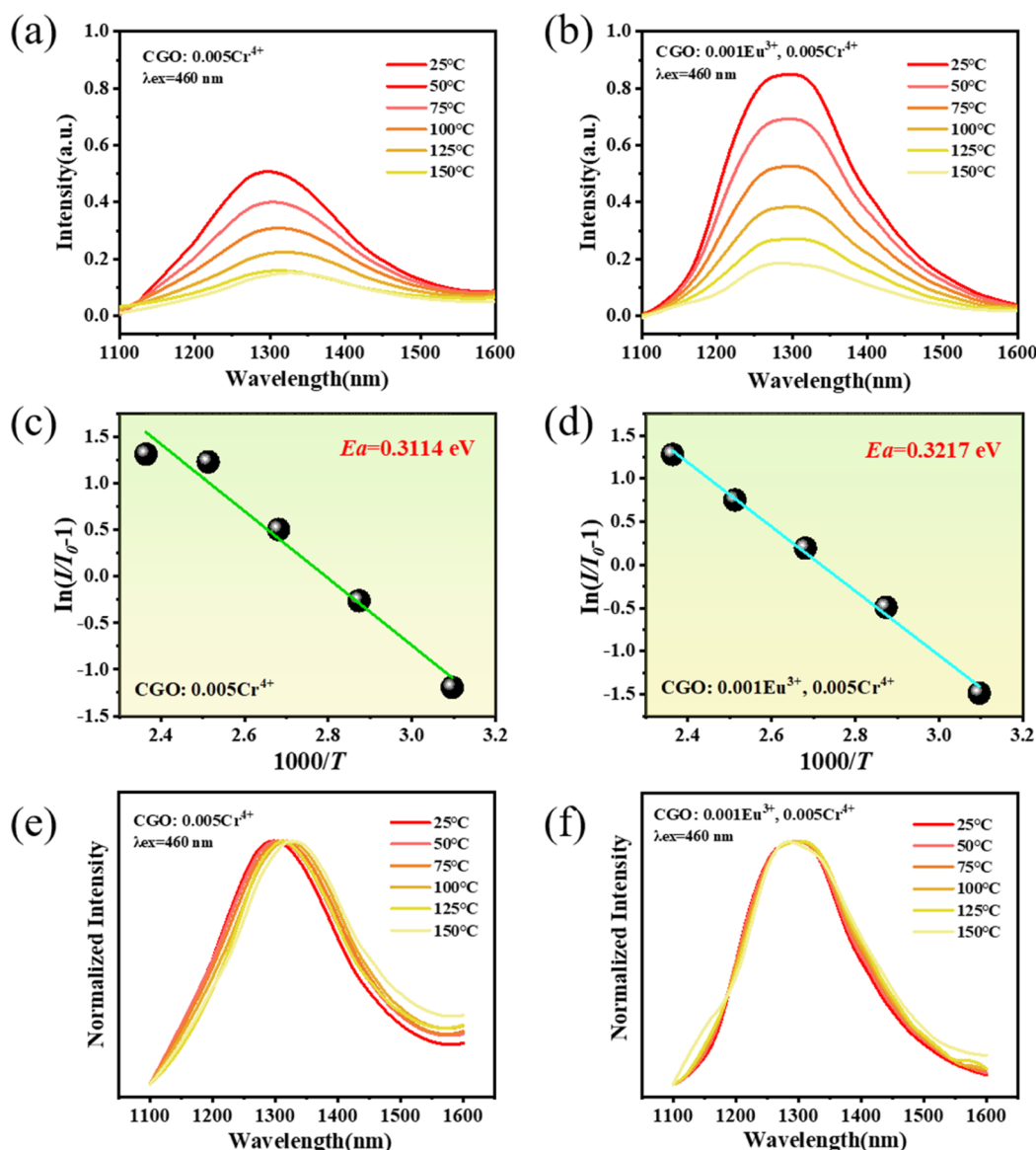**Figure 9.** Schematic diagram of the energy-transfer mechanism from Eu^{3+} to Cr^{4+} in the CGO host.

Figure 10. Temperature-dependent PL spectra of (a) CGO: $0.005Cr^{4+}$ and (b) CGO: $0.001Eu^{3+}$, $0.005Cr^{4+}$. Activation energy plots using the Arrhenius equation for (c) CGO: $0.005Cr^{4+}$ and (d) CGO: $0.001Eu^{3+}$, $0.005Cr^{4+}$. Normalized temperature-dependent PL spectra of (e) CGO: $0.005Cr^{4+}$ and (f) CGO: $0.001Eu^{3+}$, $0.005Cr^{4+}$.
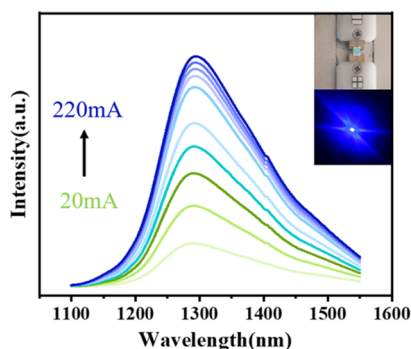
Figure 11. PL spectra of the fabricated NIR pc-LEDs under different driving currents. The illustration shows the experimental device before and after power-on.

energy transfer should be controlled by multipole interaction rather than exchange interaction, since the exchange interaction occurs at a distance less than 5 Å. The type of multipole interaction can be determined by eq 2[32,33]

$$\frac{I}{y} = K[1 + \beta(y)^{\theta/3}]^{-1} \tag{2}$$

where I refers to the sample luminescence intensity, K and β are matrix lattice constants, and y represents the doping concentration of Cr^{4+} ions. $\theta = 6$, 8, and 10 correspond to dipole–dipole, dipole–quadrupole, and quadrupole–quadrupole interactions, respectively, with $\theta = 3$ representing the energy migration between neighboring Cr^{4+} ions.[32] In Figure 4b, we show the relationship between $\log(I/y)$ and $\log(y)$. $\theta = 3.684$ can be calculated from the slope of the fitted line, which is closer to 3, indicating that the concentration quenching mechanism of Cr^{4+} ions in CGO: yCr^{4+} phosphors is mainly caused by the energy migration between neighboring ions.

Figure 3c shows the PLE and PL spectra of CGO: Eu^{3+}. The strongest excitation peak of CGO: Eu^{3+} is located between 450 and 475 nm, which is ascribed to the $^7F_0 \rightarrow {}^5D_2$ transition of

Eu^{3+} ions, which is consistent with the emission of blue chips. At 460 nm excitation, CGO: Eu^{3+} exhibits an emission spectrum composed of several small spikes at 575 nm ($^5D_0 \rightarrow$ $^7F_0$), 600 nm ($^5D_0 \rightarrow$ $^7F_1$), 611−629 nm ($^5D_0 \rightarrow$ $^7F_2$), 653 nm ($^5D_0 \rightarrow$ $^7F_3$), and 700 nm ($^5D_0 \rightarrow$ $^7F_4$).[34−37] Among these above peaks, 622 nm ($^5D_0 \rightarrow$ $^7F_2$) of red light has the strongest emission intensity, which means the highest probability of electric dipole transition. Energy transfer from Eu^{3+} to Cr^{4+} is expected to occur based on the significant overlaps with the PLE spectrum of CGO: Cr^{4+} (Figure 3b) and the PL spectrum of CGO: Eu^{3+} (Figure 3c).

3.3. Luminescence Properties of Codoped CGO.
PLE and PL spectra of CGO: Eu^{3+}, Cr^{4+} are shown in Figure 3d. Under blue light excitation at 460 nm, the codoped sample presents a broad NIR emission band with a peak at 1290 nm. It is found that the PLE spectra of CGO: Eu^{3+}, Cr^{4+} is very similar to that of CGO: Eu^{3+} at 622 nm emission, indicating that Eu^{3+} enters the CGO matrix. Furthermore, a series of Cr^{4+}-doped NIR phosphors have been compared with CGO: Eu^{3+}, Cr^{4+}, and the luminescence properties and application fields have been summarized in Table 2. Broadband spectroscopy and longer wavelength of CGO: Eu^{3+}, Cr^{4+} demonstrate the great potential for applications in organic detection and fluorescence imaging.

Figure S1 shows the PL spectra for different Eu^{3+} doping concentrations in the CGO matrix. The optimal doping is $x =$ 0.009, on which the codoping experiment with Cr^{4+} is conducted. Figure 5a depicts the NIR and visible PL spectra of CGO: 0.009Eu^{3+}, yCr^{4+} ($0 \leq y \leq 0.013$) at 460 nm excitation. The typical emission of Eu^{3+} can be observed at low Cr^{4+} doping concentration, and it starts to decrease until it vanishes with further doping. Figure 5b clearly illustrates the variation of Eu^{3+} and Cr^{4+} luminescence intensity. With the increase of Cr^{4+} content, the luminescence intensity of Eu^{3+} (peak at 622 nm) decreases monotonically, while the luminescence intensity of Cr^{4+} (peak at 1290 nm) ascends continuously until $y =$ 0.005 and then decreases due to the concentration quenching effect of Cr^{4+} ions. These changes indicate an energy-transfer process from Eu^{3+} to Cr^{4+}.

In order to verify the influence of the doped sensitizer ion Eu^{3+} on the luminescence performance, a series of CGO: xEu^{3+}, 0.005Cr^{4+} ($0 \leq x \leq 0.006$) phosphors were synthesized, whose emission spectra are shown in Figure 6. Although the doping concentration of Cr^{4+} is fixed, the luminescence intensity clearly increases with the doping amount of Eu^{3+} and reaches a maximum at $x =$ 0.001, where the intensity of Cr^{4+} enhanced by nearly two times. In addition, the NIR QYs of CGO: 0.005Cr^{4+}, and CGO: 0.001Eu^{3+}, 0.005Cr^{4+} at 460 nm excitation are 23.16% and 41.32%, respectively. The addition of sensitizer ion Eu^{3+} increases the internal quantum yield of the phosphor, which is consistent with the variation in luminescence intensity. These results verify the positive effect of Eu^{3+} in enhancing the emission intensity of Cr^{4+} through energy transfer.

3.4. Energy-Transfer Mechanism of CGO: Eu^{3+}, Cr^{4+}.
For CGO: 0.009Eu^{3+}, yCr^{4+} ($0 \leq y \leq 0.011$), the energy-transfer efficiency from Eu^{3+} ions to Cr^{4+} ions can be obtained by formula 3[39]

$$\eta E_T = 1 - I/I_0 \tag{3}$$

where I_0 and I denote the luminescence intensity of Eu^{3+} without and with Cr^{4+}, respectively. The results suggest that the energy-transfer efficiency is positively correlated with the

increment of Cr^{4+} (Figure 7b). The η_{ET} value continuously increases with the increase of the Cr^{4+} content and reaches 70% when the Cr^{4+} concentration is 0.011, indicating that the energy transfer between Eu^{3+} and Cr^{4+} is efficient.

The fluorescence decay curves of CGO: 0.009Eu^{3+}, yCr^{4+} ($0 \leq y \leq 0.011$) monitored at 622 nm were measured under 460 nm excitation, as shown in Figure 7a. When $y =$ 0, 0.001, 0.003, 0.005, 0.007, 0.009, and 0.011, the average lifetimes of Eu^{3+} are estimated to be 151.14, 114.74, 83.67, 71.55, 47.19, and 28.59 μs, respectively, showing a monotone decreasing trend, which proved that the energy transfer from Eu^{3+} to Cr^{4+} occurs. In addition, the decay curve of CGO: 0.009Eu^{3+} at 622 nm can be fitted by a double exponential function, while the codoped samples are closer to a triple exponential rule. The energy-transfer efficiency can be calculated using the decay lifetime and expressed as eq 4[40]

$$\eta_{ET} = 1 - \tau/\tau_0 \tag{4}$$

τ_0 and τ represent the fluorescence lifetime of Eu^{3+} when Eu^{3+} doped and codoped with Cr^{4+}, respectively. The calculated results obtained by formulas 3 and (4) are shown in Figure 7b. The maximum energy-transfer efficiency value is about 81%.

According to the Reisfeld approximation and Dexter's energy-transfer theory of multipolar interaction, the energy transfer of Eu$^{3+} \rightarrow$ Cr^{4+} occurs through electric multipolar interactions, which can be acquired using eq 5[41]

$$\frac{I_0}{I} \propto C^{n/3} \tag{5}$$

where I_0 and I represent the luminescence intensity of Eu^{3+} in the absence and presence of Cr^{4+}, C is the total concentration of Eu^{3+} and Cr^{4+}, and $n =$ 6, 8, and 10 correspond to dipole−dipole, dipole−quadrupole, and quadrupole−quadrupole interactions, respectively. To obtain the value of n, we show the relationship between I_0/I and $C^{n/3}$ in Figure 8. The best linear is fitted with $n =$ 6 ($R^2 =$ 0.9757), so the energy transfer from Eu^{3+} to Cr^{4+} in the CGO host is dominated by the dipole−dipole mechanism.

In order to describe the energy-transfer mechanism from Eu^{3+} to Cr^{4+}, a schematic energy level diagram is used to describe the relevant processes in detail. As shown in Figure 9, upon 460 nm blue light excitation, the electrons of Eu^{3+} and Cr^{4+} transition from the ground state to the excited state [Eu^{3+}: $^7F_0 \rightarrow$ $^5D_2$; Cr^{4+}: $^3A_2 \rightarrow$ $^3T_1$(^3P)]. For Eu^{3+}, the excited electrons reach the $^5D_0$ energy level nonradiatively. Some electrons return to the ground state with a radiative process through $^5D_2 \rightarrow$ ^7F_J ($J =$ 0, 1, 2, 3, 4) transition. Meanwhile, the electrons of Eu^{3+} ions at the $^5D_0$ level transfer energy to Cr^{4+} ions through the resonance process. For Cr^{4+}, after the blue light excitation and energy-transfer process, enhanced characteristic NIR emission occurs through the $^3T_2 \rightarrow$ $^3A_2$ transition. In conclusion, the energy-transfer effect of Eu$^{3+} \rightarrow$ Cr^{4+} finally produces the superposition of NIR spectra, which enables Cr^{4+} ions to emit NIR light with higher intensity.

3.5. Temperature-Dependent PL Properties and Packing Performance.
Thermal stability of luminescence is an important indicator for evaluating the performance and characterizing the practical application of fluorescent powder. The temperature-dependent PL spectra of CGO: 0.005Cr^{4+} and CGO: 0.001Eu^{3+}, 0.005Cr^{4+} were monitored from 25 to 150 °C under 460 nm excitation. As shown in Figure 10a,b, thermal quenching behavior occurred in both samples.

To further understand the thermal quenching phenomenon, the activation energy (E_a) of CGO: 0.005Cr^{4+} and CGO: 0.001Eu^{3+}, 0.005Cr^{4+} can be evaluated by Arrhenius equation[42,43]

$$I_T = \frac{I_0}{1 + C \times \exp\left(\frac{-E_a}{KT}\right)} \tag{6}$$

where I_0 and I_T represent the emission intensity at room temperature (25 °C) and temperature T, respectively, C is a constant of the given host lattice, and K is Boltzmann's constant. The linear fitting relationship between $\ln(I_0/I - 1)$ and $1000/T$ (Figure 10c,d) calculates that the thermal quenching activation energies of CGO: 0.005Cr^{4+} and CGO: 0.001Eu^{3+}, 0.005Cr^{4+} are 0.3114 and 0.3217 eV, respectively. The activation energy of thermal quenching can be used to judge the thermal stability of the sample. At high E_a, thermal quenching is difficult to occur. What is more, as shown in Figure 10e,f, the emission spectra of CGO: 0.005Cr^{4+} and CGO: 0.001Eu^{3+}, 0.005Cr^{4+} at different temperatures are normalized. With the increase of temperature, the spectral shape of CGO: 0.005Cr^{4+} does not change, but the emission peak is shifted to the long wavelength direction, indicating that the crystal field strength is gradually decreasing and the thermal stability is poor. The spectral shape and position of CGO: 0.001Eu^{3+}, 0.005Cr^{4+} almost does not change with temperature, indicating better thermal stability than CGO: 0.005Cr^{4+}.

Typically, thermal stability of phosphor is closely related to multiple doped ions and lattice distortions. The combination of Eu^{3+} can increase the thermal quenching activation of the material, resulting in improved thermal stability. This is because the smaller radius of Eu^{3+} than that of Ca^{2+} forms a volume compensation, which alleviates the Cr^{4+} lattice expansion and reduces the energy of the system. It can be seen that the doping of sensitizer Eu^{3+} not only enhances the NIR luminescence of Cr^{4+} but also has a positive effect on the thermal stability of the material.

CGO: 0.001Eu^{3+}, 0.005Cr^{4+} phosphor and a 460 nm commercial InGaN chip were fabricated to produce a broadband NIR luminescence device. Figure 11 shows a strong NIR band in the emission spectrum. The inset image displays the experimental device before and after power-on. As the driving current continues to increase, the luminescence intensity of the pc-LED device monotonically increases. The maximum output power of 31.4 mW is obtained at a current injection of 220 mA. Moreover, the spectral half-width of CGO: 0.001Eu^{3+}, 0.005Cr^{4+} is wider (∼200 nm) than that of the NIR LED chip, which can meet more application requirements, demonstrating the potential of CGO: Eu^{3+}, Cr^{4+} as a long-wavelength broadband NIR phosphor for NIR light source applications.

4. CONCLUSIONS

In summary, a series of CGO: xEu^{3+}, yCr^{4+} NIR phosphors have been prepared by high-temperature solid-state reactions. It is determined that Cr preferentially replaces the tetrahedral Ge site and Eu randomly occupies the octahedral Ca site according to XRD patterns and valence equilibrium and proximity of ionic radius. For the CGO: Eu^{3+} phosphor, the highest intensity of 622 nm red light is generated under the excitation of 460 nm blue chips, which overlaps with the excitation peak of CGO: Cr^{4+} from $^3A_2 \rightarrow {}^3T_1({}^3F)$ transition

and can be used as another energy channel of Cr^{4+}-doped phosphor. CGO: Eu^{3+}, Cr^{4+} phosphors exhibit a broad band of NIR emission centered at 1290 nm spanning 1100−1600 nm. Due to the energy transfer from Eu^{3+} to Cr^{4+}, the luminescence intensity and quantum efficiency of Cr^{4+} are enhanced by nearly two times. In the CGO host, the energy-transfer mechanism of Eu$^{3+} \rightarrow$ Cr^{4+} is the dipole−dipole interaction. The emission spectra and decay lifetime curves indicate that the phosphors have a high energy-transfer efficiency of up to 81%. Moreover, the doping of Eu^{3+} increases the thermal activation energy of CGO: Eu^{3+}, Cr^{4+}, and the thermal stability is also improved. Finally, the CGO: Eu^{3+}, Cr^{4+} phosphor with the highest luminescence intensity is coated on the surface of a 460 nm blue chip and fabricated into a NIR pc-LED, which achieves a maximum output power of 31.4 mW at 220 mA driving current. Proper output power and wider half-width than the NIR LED chip demonstrate the potential of NIR pc-LEDs in the application of long-wavelength broadband NIR light sources.

■ ASSOCIATED CONTENT

ⓈⅠ Supporting Information

The Supporting Information is available free of charge at https://pubs.acs.org/doi/10.1021/acsomega.3c00995.

> PL spectra of CGO: xEu^{3+} ($0 \leq x \leq 0.013$) and concentration dependence of peak intensity at 622 nm (PDF)

■ AUTHOR INFORMATION

Corresponding Author

Yuanhong Liu − *National Engineering Research Center for Rare Earth, General Research Institute for Nonferrous Metals, and GRIREM Advanced Materials Co., Ltd, Beijing 100088, People's Republic of China;* ⓞ orcid.org/0000-0001-6370-2614; Email: liuyuanhonggrinm@163.com

Authors

Shuya He − *National Engineering Research Center for Rare Earth, General Research Institute for Nonferrous Metals, and GRIREM Advanced Materials Co., Ltd, Beijing 100088, People's Republic of China*

Tongyu Gao − *National Engineering Research Center for Rare Earth, General Research Institute for Nonferrous Metals, and GRIREM Advanced Materials Co., Ltd, Beijing 100088, People's Republic of China*

Ronghui Liu − *National Engineering Research Center for Rare Earth, General Research Institute for Nonferrous Metals, and GRIREM Advanced Materials Co., Ltd, Beijing 100088, People's Republic of China*

Guantong Chen − *National Engineering Research Center for Rare Earth, General Research Institute for Nonferrous Metals, and GRIREM Advanced Materials Co., Ltd, Beijing 100088, People's Republic of China*

Mobin Duan − *National Engineering Research Center for Rare Earth, General Research Institute for Nonferrous Metals, and GRIREM Advanced Materials Co., Ltd, Beijing 100088, People's Republic of China*

Min Cao − *National Engineering Research Center for Rare Earth, General Research Institute for Nonferrous Metals, and GRIREM Advanced Materials Co., Ltd, Beijing 100088, People's Republic of China*

Complete contact information is available at:

https://pubs.acs.org/10.1021/acsomega.3c00995

REFERENCES

(1) Liu, F.; Liang, Y.; Chen, Y.; Pan, Z. Divalent Nickel-Activated Gallate-Based Persistent Phosphors in the Short-Wave Infrared. *Adv. Opt. Mater.* **2016**, *4*, 562−566.

(2) Qiao, J.; Zhang, S.; Zhou, X.; Chen, W.; Gautier, R.; Xia, Z. Near-Infrared Light-Emitting Diodes utilizing a Europium-Activated Calcium Oxide Phosphor with External Quantum Efficiency of up to 54.7%. *Adv. Mater.* **2022**, *34*, 2201887.

(3) Yang, F.; Zhang, Q.; Huang, S.; Ma, D. Recent advances of near infrared inorganic fluorescent probes for biomedical applications. *J. Mater. Chem. B* **2020**, *8*, 7856−7879.

(4) Hong, G.; Diao, S.; Antaris, A. L.; Dai, H. Carbon Nanomaterials for Biological Imaging and Nanomedicinal Therapy. *Chem. Rev.* **2015**, *115*, 10816−10906.

(5) Nanai, Y.; Ishida, R.; Urabe, Y.; Nishimura, S.; Fuchi, S. Octave-spanning broad luminescence of Cr^{3+}, Cr^{4+}-codoped Mg_2SiO_4 phosphor for ultra-wideband near-infrared LEDs. *Jpn. J. Appl. Phys.* **2019**, *58*, SFFD02.

(6) Wang, C.; Zhang, Y.; Han, X.; Hu, D.; He, D.; Wang, X.; Jiao, H. Energy transfer enhanced broadband near-infrared phosphors: Cr^{3+}/Ni^{2+} activated $ZnGa_2O_4$-Zn_2SnO_4 solid solutions for the second NIR window imaging. *J. Mater. Chem. C* **2021**, *9*, 4583−4590.

(7) Huang, S.; Yan, Y.; Shang, M.; Wang, Y.; Sun, Y.; Dang, P.; Lin, J. Super Broadband Near-Infrared Solid Solution Phosphors with Adjustable Peak Wavelengths from 1165 to 875 nm for NIR Spectroscopy Applications. *Adv. Opt. Mater.* **2022**, *11*, 2202291.

(8) Yan, Y.; Shang, M.; Huang, S.; Wang, Y.; Sun, Y.; Dang, P.; Lin, J. Photoluminescence Properties of $AScSi_2O_6$:Cr^{3+} (A = Na and Li) Phosphors with High Efficiency and Thermal Stability for Near-Infrared Phosphor-Converted Light-Emitting Diode Light Sources. *ACS Appl. Mater. Interfaces* **2022**, *14*, 8179−8190.

(9) Liu, G.; Molokeev, M. S.; Xia, Z. Structural Rigidity Control toward Cr^{3+}-Based Broadband Near-Infrared Luminescence with Enhanced Thermal Stability. *Chem. Mater.* **2022**, *34*, 1376−1384.

(10) Kück, S. Laser-related spectroscopy of ion-doped crystals for tunable solid-state lasers. *Appl. Phys. B* **2001**, *72*, 515−562.

(11) Tanabe, Y.; Sugano, S. On the Absorption Spectra of Complex Ions II. *J. Phys. Soc. Jpn.* **1954**, *9*, 766−779.

(12) Hazenkamp, M. F.; Oetliker, U.; Güdel, H.; Kesper, U.; Reinen, D. Absorption and luminescence spectroscopy of Cr^{4+}-doped Ca_2GeO_4. A potential near infrared laser material. *Chem. Phys. Lett.* **1995**, *233*, 466−470.

(13) Redhammer, G. J.; Roth, G.; Amthauer, G.; Lottermoser, W. On the crystal chemistry of olivine-type germanate compounds, $Ca_{1+x}M_{1-x}GeO_4$ (M^{2+} = Ca, Mg, Co, Mn). *Acta Crystallogr., Sect. B: Struct. Sci.* **2008**, *64*, 261−271.

(14) Zhao, F.; Song, Z.; Liu, Q. Advances in Chromium-Activated Phosphors for Near-Infrared Light Sources. *Laser Photon. Rev.* **2022**, *16*, 2200380.

(15) Bykov, A. B.; Petricevic, V.; Steiner, J.; Yao, D.; Isaacs, L. L.; Kokta, M. R.; Alfano, R. Flux growth and characterization of Cr^{4+}: Ca_2GeO_4 crystals as a new near infrared tunable laser material. *J. Cryst. Growth* **2000**, *211*, 295−301.

(16) Hazenkamp, M. F.; Güdel, H. U.; Atanasov, M.; Kesper, U.; Reinen, D. Optical spectroscopy of Cr^{4+}-doped Ca_2GeO_4 and Mg_2SiO_4. *Phys. Rev. B: Condens. Matter Mater. Phys.* **1996**, *53*, 2367−2377.

(17) Petricevic, V.; Gayen, S. K.; Alfano, R. R.; Yamagishi, K.; Anzai, H.; Yamaguchi, Y. Laser action in chromium-doped forsterite. *Appl. Phys. Lett.* **1988**, *52*, 1040−1042.

(18) Li, C.; Xu, J.; Liu, W.; Zheng, D.; Zhang, S.; Zhang, Y.; Lin, H.; Liu, L.; Liu, J.; Zeng, F. Synthesis and characterization of Cr^{4+}-doped Ca_2GeO_4 tunable crystal. *J. Alloys Compd.* **2015**, *636*, 211−215.

(19) Chen, X.; Liu, S.; Huang, K.; Nie, J.; Kang, R.; Tian, X.; Zhang, S.; Li, Y.; Qiu, J. Cr^{4+} activated NIR-NIR multi-mode luminescent nanothermometer for double biological windows. *Chem. Eng. J.* **2020**, *396*, 125201.

(20) Wang, X.; Wang, Z.; Zheng, M.; Cui, J.; Yao, Y.; Cao, L.; Zhang, M.; Yang, Z.; Suo, H.; Li, P. A dual-excited and dual near-infrared emission phosphor $Mg_{14}Ge_5O_{24}$: Cr^{3+}, Cr^{4+} with a super broad band for biological detection. *Dalton Trans.* **2021**, *50*, 311−322.

(21) Zhou, H.; Cai, H.; Zhao, J.; Song, Z.; Liu, Q. Crystallographic control for Cr^{4+} activators toward efficient NIR-II luminescence. *Inorg. Chem. Front.* **2022**, *9*, 1912−1919.

(22) Ye, Z.; Wang, Z.; Yang, H.; Huo, X.; Wang, Y.; Wu, Q.; Wang, D.; Zhao, J.; Suo, H.; Li, P. A non-rare earth ion doped broadband emission phosphor located in NIR-II for ethanol concentration detection. *Dalton Trans.* **2022**, *51*, 13499−13506.

(23) Guo, H.; Wang, T.; Liu, B.; Gao, W.; Xiu, L.; Cui, Z.; Zhang, H.; Ma, Q.; Wang, S.; Li, Z.; et al. Fabrication and photoluminescence characteristics of novel red-emitting Ba_2LuNbO_6:Eu^{3+} double-perovskite phosphors on near UV WLEDs. *J. Rare Earths* **2022**, *40*, 1173−1180.

(24) Xu, Y.; Li, G.; Guan, X.; Wei, Y.; Zhang, M. Synthesis, crystal structure and photoluminescence properties of novel double perovskite La_2CaSnO_6:Eu^{3+} red-emitting phosphors. *J. Rare Earths* **2022**, *40*, 1682−1690.

(25) Dai, T.; Ju, G.; Lv, Y.; Jin, Y.; Wu, H.; Hu, Y. Luminescence properties of novel dual-emission (UV/red) long afterglow phosphor $LiYGeO_4$: Eu^{3+}. *J. Lumin.* **2021**, *237*, 118193.

(26) Toby, B. H. EXPGUI, a graphical user interface for GSAS. *J. Appl. Crystallogr.* **2001**, *34*, 210−213.

(27) Shannon, R. D.; Prewitt, C. T. Effective ionic radii in oxides and fluorides. *Acta Crystallogr., Sect. B: Struct. Crystallogr. Cryst. Chem.* **1969**, *25*, 925−946.

(28) Veremeichik, T. F.; Zharikov, E. V.; Subbotin, K. A. New laser crystals of complex oxides doped with ions of d elements with variable valence and different structural localization. Review. *Crystallogr. Rep.* **2003**, *48*, 974−988.

(29) Su, B.; Geng, S.; Xiao, Z.; Xia, Z. Highly Distorted Antimony(III) Chloride $[Sb_2Cl_8]^{2-}$ Dimers for Near-Infrared Luminescence up to 1070 nm. *Angew. Chem., Int. Ed.* **2022**, *61*, 202208881.

(30) Dexter, D. L.; Schulman, J. H. Theory of Concentration Quenching in Inorganic Phosphors. *J. Chem. Phys.* **1954**, *22*, 1063−1070.

(31) Blasse, G. Energy Transfer in Oxidic Phosphors. *Phys. Lett. A* **1968**, *28*, 444−445.

(32) Van Uitert, L. G.; Johnson, L. F. Energy Transfer Between Rare-Earth Ions. *J. Chem. Phys.* **1966**, *44*, 3514−3522.

(33) Van Uitert, L. G. Characterization of Energy Transfer Interactions between Rare Earth Ions. *J. Electrochem. Soc.* **1967**, *114*, 1048−1053.

(34) Koseva, I.; Tzvetkov, P.; Ivanov, P.; Petrova, P.; Tomova, R.; Nikolov, V. Photoluminescent properties of europium doped calcium orthogermanate (Ca_2GeO_4) as a candidate for Red phosphor. *Optik* **2020**, *205*, 164269.

(35) Loos, S.; Steudel, F.; Ahrens, B.; Schweizer, S. Temperature-dependent luminescence and energy transfer properties of Tb^{3+} and Eu^{3+} doped barium borate glasses. *J. Lumin.* **2017**, *181*, 31−35.

(36) Wang, X.; Zhao, S.; Zhang, Y.; Sheng, G. Controlled synthesis and tunable luminescence of $NaYF_4$: Eu^{3+}. *J. Rare Earths* **2010**, *28*, 222−224.

(37) Xu, C.; Li, Y.; Huang, Y.; Yu, Y. M.; Seo, H. J. Luminescence characteristics and site-occupancy of Eu^{2+}- and Eu^{3+}-doped $MgZn_2(PO_4)_2$ phosphors. *J. Mater. Chem.* **2012**, *22*, 5419−5426.

(38) Cai, H.; Chen, H.; Zhou, H.; Zhao, J.; Song, Z.; Liu, Q. Controlling Cr^{3+}/Cr^{4+} concentration in single-phase host toward tailored super-broad near-infrared luminescence for multifunctional applications. *Mater. Today Chem.* **2021**, *22*, 100555.

(39) Deng, B.; Liu, S.; Zhou, C. S.; Liu, H.; Chen, J.; Yu, R. Eu^{3+}-Activated $Gd_8V_2O_{17}$: Energy Transfer, Luminescence, and Temperature-Dependence Characteristics. *Chemistry* **2018**, *24*, 11627−11636.

(40) Guo, S.; Zhang, S.; Mu, Z.; Wu, F.; Feng, X.; Zhang, Q.; Feng, J.; Zhu, D.; Du, Q. Enhanced near infrared luminescence of Lu_2GeO_5: Nd^{3+} by the co-doping of Bi^{3+}. *J. Lumin.* **2019**, *206*, 278−283.

(41) Dexter, D. L. A Theory of Sensitized Luminescence in Solids. *J. Chem. Phys.* **1953**, *21*, 836−850.

(42) Zhong, J.; Chen, D.; Yuan, Y.; Chen, L.; Yu, H.; Ji, Z. Synthesis and spectroscopic investigation of $Ba_3La_6(SiO_4)_6$: Eu^{2+} green phosphors for white light-emitting diodes. *Chem. Eng. J.* **2017**, *309*, 795−801.

(43) Dang, P.; Liang, S.; Li, G.; Lian, H.; Shang, M.; Lin, J. Broad color tuning of Bi^{3+}/Eu^{3+}-doped $(Ba,Sr)_3Sc_4O_9$ solid solution compounds via crystal field modulation and energy transfer. *J. Mater. Chem. C* **2018**, *6*, 9990−9999.